

Approximating nonlinear forces with phase-space decoupling

B Folsom* and E Laface†
European Spallation Source, ERIC
Lund, Sweden
 (Dated: June 17, 2022)

Beam tracking software for accelerators can be divided into two categories: fast envelope simulations limited to linear beam optics, and slower multiparticle simulations that can model nonlinear effects. To find a middle ground between these approaches, we introduce virtual parameters in position and momentum which exhibit a cross-dependency (i.e. $x^* = f(p_0)$ where p_0 is an initial momentum and x^* virtual projection of position onto the momentum axis). This technique approximates multiparticle results with a significant ($\sim 10\%$) reduction in calculation cost, while also allowing for the envelope simulation of non-linear forces.

PACS numbers: 02.20.5v, 29.27.-a, 41.85.-p, 05.10.-a, 05.45.-a

I. INTRODUCTION

The software for predicting and correcting beam dynamics in real time is largely dependent on approximations that treat the phase-space density as a single envelope. Such methods are computationally efficient, but rely on a linearization of beam optics to preserve symplecticity.

Conversely, modern multiparticle tracking codes can account for non-linear forces (i.e. octupole errors/magnets), but are generally so CPU-intensive that they must be used offline, making them ill-suited for diagnostics and troubleshooting.

In developing the ESS Linac Simulation (ELS) software, our group seeks a compromise between these two approaches. That is, we intend to implement real-time, non-linear beam tracking requiring only the processing power of a desktop machine or small local cluster.

Expanding on prior works [1, 2], we now introduce an optimization method for non-linear tracking by using “virtual” phase-space coordinates that allow for the independent calculation of position and momentum densities. It is important to classify these coordinates as non-physical: they are derived assuming a cross-dependency exists (e.g. $x^* = f(p_0)$, where x^* and p_0 are virtual position and real momentum, respectively).

When used in conjunction with standard techniques for multiparticle tracking, these virtual coordinates allow for the use of monovariate polynomials, which present a significant reduction in the number of required calculations when compared with the bivariate multiplications normally needed.

This approach is also shown to be applicable when used in an envelope code, thus providing a coarse approximation of non-linear forces for real-time tracking.

II. THEORY

For simplicity, we will only consider transverse motion in the horizontal plane from an initial Gaussian distribution. That is, we assume that the distribution’s vertical emittance is small enough to treat the Hamiltonians governing motion in the x and y directions as uncoupled.

The starting point for this method, outlined in Ref. [1], involves taking particle count N as an invariant as the position and momentum envelopes ρ_x and ρ_p evolve:

$$\int \rho_x^L dx_L = \int \rho_x^0 dx_0 = \int \rho_p^L dp_L = \int \rho_p^0 dp_0 = N. \quad (1)$$

where ρ_x^L and ρ_x^0 are the respective final and initial position densities, and likewise for the momentum densities.

To exploit this identity, ρ_x^L must be independent of p_0 . This can be accomplished using the approximation [3, 4]

$$p_0 \approx -\frac{\alpha}{\beta} x_0, \quad (2)$$

where α and β are the well-known Twiss parameters. This leads to the equation

$$\rho_x^L = \frac{\rho_x^0}{\left| \frac{\partial x_L}{\partial x_0} \right|}. \quad (3)$$

Here, the partial derivative in the denominator is the Jacobian in 1D. Unfortunately, this approximation is only valid if the previous history of the beam is linear (thus maintaining elliptical phase space). Since we want an algorithm that remains accurate for iterated nonlinear kicks, a new approximation is needed.

To proceed, we try adding the constraint that the initial distribution is Gaussian in both x and p , this allows us to solve Eq. 1 for x_0 and p_0 .

$$\int \rho_x^0 dx_0 = \int \rho_p^0 dp_0 \quad (4)$$

$$\frac{1}{2} \operatorname{erf} \left(\frac{\sqrt{2} x_0}{2 \sigma_{x_0}} \right) = \frac{1}{2} \operatorname{erf} \left(\frac{\sqrt{2} p_0}{2 \sigma_{p_0}} \right),$$

* ben.folsom@esss.se; Also at High-Energy Physics Division, Lund University.

† emanuele.laface@esss.se

which yields

$$p_0 = \sqrt{2}\sigma_{p_0} \operatorname{erfinv} \left(\operatorname{erf} \left(\frac{\sqrt{2}x_0}{2\sigma_{x_0}} \right) \right) = x_0 \frac{\sigma_{p_0}}{\sigma_{x_0}}. \quad (5)$$

This solution does produce a bigaussian phase-space ellipse, but is unsuitable for approximating p_0 with distributions of an irregular shape.

We continue by guessing that a solution exists for $p_0 = f(x_0)$ for irregularly shaped distributions. Denoting these solutions as p^* and ρ_p^* for momentum and momentum density, respectively, we have

$$\int \rho_p^*(p_0) dp^*(x_0) = \int \rho_p^0 dp_0, \quad (6)$$

where it is critical to note that p^* is solely dependent on x_0 , while ρ_p^* remains a function of p_0 .

With the left-hand-side integrand and integration variables decoupled, it follows (for both x^* and p^*):

$$N = x^* \rho_x^* = \int \rho_x^0 dx_0 \quad (7)$$

$$N = p^* \rho_p^* = \int \rho_p^0 dp_0.$$

Again exploiting particle-count invariance and squaring N , we can assert that

$$N^2 = \mathcal{C} = \rho_x^* \rho_p^* x^* p^*, \quad (8)$$

and thus

$$\frac{d}{dx_0} \mathcal{C} + \frac{d}{dp_0} \mathcal{C} = 0. \quad (9)$$

We can then simplify, treating all p_0 -dependent terms as $f(p_0)$:

$$\begin{aligned} 0 &= \frac{d}{dx_0} \mathcal{C} + \frac{d}{dp_0} \mathcal{C} \\ &= \frac{\partial \rho_x^I}{\partial x_0} (\rho_p^I x^* p^*) + \frac{\partial p^*}{\partial x_0} (\rho_x^I \rho_p^I x^*) + f(p_0) \\ &= \frac{\partial \rho_x^I}{\partial x_0} \left(\int \rho_p^0 dp_0 x^* \right) \\ &\quad + \frac{\partial p^*}{\partial x_0} \left(\int \rho_x^0 dx_0 \frac{\int \rho_p^0 dp_0}{p^*} \right) + f(p_0). \end{aligned} \quad (10)$$

Then, dividing by $\int \rho_p^0 dp_0$

$$\begin{aligned} 0 &= \frac{\partial \rho_x^I}{\partial x_0} x^* + \frac{\partial p^*}{\partial x_0} \frac{1}{p^*} \int \rho_x^0 dx_0 + f(p_0) \\ &= \frac{\partial \rho_x^I}{\partial x_0} x^* + \frac{\partial p^*}{\partial x_0} \frac{1}{p^*} x^* \rho_x^I + f(p_0) \\ &= \left(\frac{\partial \rho_x^I}{\partial x_0} + \frac{\partial p^*}{\partial x_0} \frac{1}{p^*} \rho_x^I \right) + f(p_0). \end{aligned} \quad (11)$$

Assuming a solution exists about $p_0 = 0$, we find

$$\begin{aligned} \frac{\partial \rho_x^I}{\partial x_0} &\approx -\frac{\partial p^*}{\partial x_0} \frac{\rho_x^I}{p^*} \\ \frac{1}{\rho_x^I} \frac{\partial \rho_x^I}{\partial x_0} &\approx -\frac{\partial p^*}{\partial x_0} \frac{1}{p^*} \\ \frac{x^*}{\int \rho_x^0 dx_0} \frac{\rho_x^0}{x^*} &\approx -\frac{\partial p^*}{\partial x_0} \frac{1}{p^*}. \end{aligned} \quad (12)$$

We can again solve for a Gaussian initial distribution, noting that $\frac{\partial p^*}{\partial x}$ is not constant, in contrast with Eq. 5.

$$\frac{\partial p^*}{\partial x_0} = -p^* \frac{\rho_x^0}{\int \rho_x^0 dx_0} \equiv -\frac{p^* \rho_x^0}{\Upsilon_x}, \quad (13)$$

where the placeholder in the denominator is defined as

$$\Upsilon_x \equiv \frac{1}{2} \operatorname{erf} \left(\frac{\sqrt{2}x_0}{2\sigma_x} \right). \quad (14)$$

A similar placeholder in terms of initial momentum will be used presently:

$$\Upsilon_p \equiv \frac{1}{2} \operatorname{erf} \left(\frac{\sqrt{2}p_0}{2\sigma_p} \right). \quad (15)$$

We now check the following solutions:

$$\begin{aligned} p^* &= -\exp \left\{ -\frac{\rho_x^0}{\Upsilon_x} x_0 \right\} \mathcal{C} \\ x^* &= -\exp \left\{ -\frac{\rho_p^0}{\Upsilon_p} p_0 \right\} \mathcal{D}. \end{aligned} \quad (16)$$

To solve for \mathcal{C} and \mathcal{D} , we normalize to Eq. 5, treating it as an uncoupled solution (i.e. where $p^* = p_0$).

$$\begin{aligned} p_0 &= x_0 \frac{\sigma_p}{\sigma_x} = \mathcal{C} \\ x_0 &= p_0 \frac{\sigma_x}{\sigma_p} = \mathcal{D}. \end{aligned} \quad (17)$$

Substituting these two expressions into Eq. 16 we have

$$p^* = -\exp \left(-\frac{\rho_x^0}{\Upsilon_x} x_0 \right) x_0 \frac{\sigma_p}{\sigma_x} \quad (18)$$

$$x^* = -\exp \left(-\frac{\rho_p^0}{\Upsilon_p} p_0 \right) p_0 \frac{\sigma_x}{\sigma_p}. \quad (19)$$

At this point, the x_L in Eq. 3 can be calculated using an exponential Lie-operator method [5]:

$$x_L(x_0, p^*) = \{ \exp [-L : \mathcal{H}(x_0, p_0) :] x_0 \} |_{p_0 \rightarrow p^*}. \quad (20)$$

where L is longitudinal displacement and the Hamiltonian for a multipole element is

$$\mathcal{H} = \frac{ep}{m} \frac{k \cdot (x_0)^n}{n!} + \frac{(p_0)^2}{2m}. \quad (21)$$

Here, e , p , and m are the fundamental charge, reference longitudinal momentum, and particle mass, respectively; $n = 3, 4, 5, \dots$ for sextupoles, octupoles, decapoles, etc; and k [$\text{T} \cdot \text{m}^{1-n}$]. Throughout this article we use $p = 1 \text{ GeV}/c$ as a reference momentum.

In implementing Eq. 20, it is important to recognize that \mathcal{H} must be calculated symbolically first for each element (a relatively low-cost operation that can be stored in a library). Then, $p^*(x_0)$ and x_0 are substituted in at each step, reducing the bivariate $x_L(x_0, p_0)$ to a mono-variate $x_L(x_0)$.

III. MULTIPARTICLE RESULTS

As a preliminary note, a strong fit can be seen between distributions based on Eq. 19 and a Cauchy distribution (Fig. 1). Thus, x^* can be seen as a projection of x_0 onto the momentum axis. A generalization of Eq. 13 may also be of use, particularly for cases where the projected distribution is more easily parametrized than its physical counterpart.

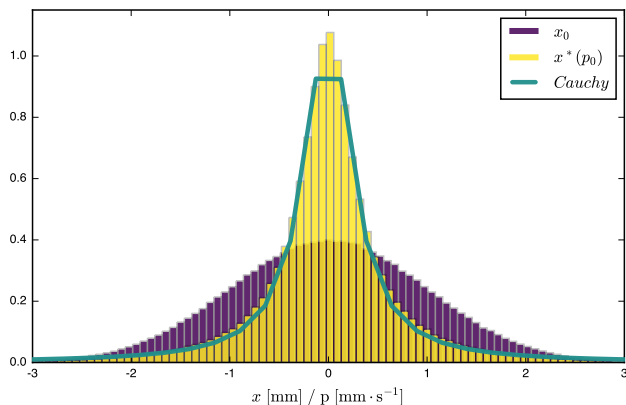


FIG. 1. Comparison of a normalized initial x_0 Gaussian distribution with its virtual x^* counterpart (using Eq. 19 with $\sigma_x = \sigma_p = 1$ [mm] and one million samples points) and a Cauchy distribution with $\gamma \approx 0.2867$ (solid line).

Before testing Eqs. 18 and 19 in terms of profile density, we can verify their accuracy by running multiparticle transformations with and without the new virtual variables.

Initially, it was found that p^* and x^* are only applicable for small and large L , respectively. This trait is detailed in Table I. Note that L and k do not have compatible units. As such, the inequalities used reflect limiting cases where the effects of either L or k become negligible.

It should also be noted that, in cases where $L \approx k$, naive solutions stemming from Eq. 17,

$$p^* = x_0 \frac{\sigma_p}{\sigma_x} \quad (22)$$

TABLE I. Parameters for multiparticle transforms in 1D phase space: valid for both $x_0 \rightarrow x_L$ and $p_0 \rightarrow p_L$.

$L \gg k$	(x^*, p_0)
$L \approx k$	(x^*, p^*)
$L \ll k$	(x_0, p^*)

$$x^* = p_0 \frac{\sigma_x}{\sigma_p}, \quad (23)$$

are often more closely matched to the “unstarred” results than when using Eqs. 18 and 19 for single-kick tests. However, for multi-kick mappings, such naive approximations do not perform so well. This is illustrated in Fig. 2, which compares the full bivariate Lie transform with three p^* approximations: (Eq. 18, Eq. 22, and a $p^* = 0$ null set, respectively) in a scenario with thin octupole kicks and interspersed drift segments. Here, the magnet gradient/length parameters were chosen to be convergent in the sense that more iterations led to a more tightly wound central region.

For these tests, only x_L uses the virtualized p^* (an explicit bivariate p_L calculation is still taken at each step). Although Table I indicates that p^* is valid for mapping both x_L and p_L , the $p_L(x_0, p^*)$ mapping collapses toward zero after a few iterations. Moreover, no virtualized variables are used for the drift sections.

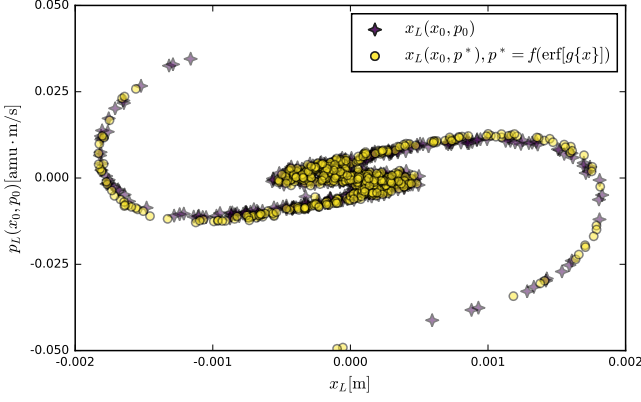
Despite this being such a conservative use of the virtual coordinates, the overall performance improvement is substantial (see Figs. 3 and 4). Here, both particle count and exponential Lie-operator (Eq. 20) series truncation order were used as dependent variables.

To compare the performance of bivariate and mono-variate polynomial multiplications, Dragt’s algorithms for truncated power-series algebra (TPSA) [5, Appendix S] were transcribed to Julia and compared against its supported TPSA packages [6]. Among these, it was found that Julia’s MultiPoly package [7] performed the necessary polynomial multiplication about 50% faster than our ad-hoc algorithm (e.g. 1540 allocations versus 2280 allocations, respectively, for a third-order multiplication).

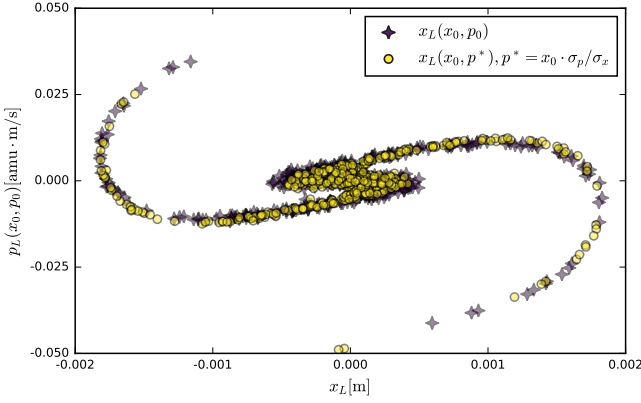
IV. ENVELOPE RESULTS

Our originally stated goal was to find a new approximation for x_L to use in Eq. 3 that does not rely on Twiss parameters, which are ill-suited for handling coupled Hamiltonians. However, as shown in Fig. 5, an approximation of

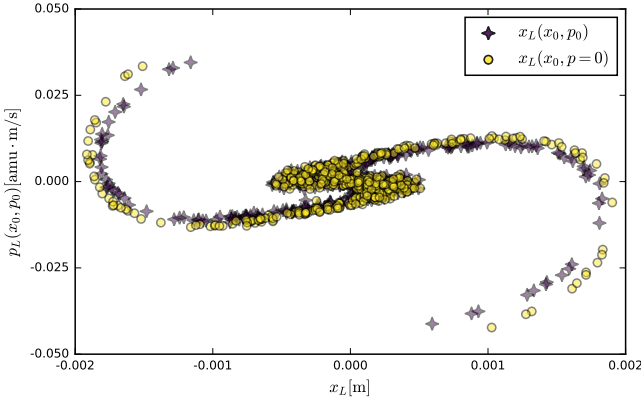
$$\rho_x^L = \frac{\rho_x^0}{\left| \frac{\partial x_L}{\partial x_0} \frac{\partial p_L}{\partial p_0} \right|_{p_0 \rightarrow p^*}} \quad (24)$$



(a) Error-function Approximation



(b) Naive Standard Deviation Approximation



(c) Null-Momentum Approximation

FIG. 2. Iterated use of Eq. 18 versus standard Lie transport results for 100,000 particles with initial Gaussian distributions of $\sigma_x = \sigma_p = 1$ mm (a). Also shown are two naive p^* approximations: $p^* = x_0 \frac{\sigma_p}{\sigma_x}$ in (b) and $p^* = 0$ in (c). The transport map consists of 200 octupole-drift sections: $k = 1.93 \cdot 10^{-7}$ [T · m⁻³], $L_{oct} = 1 \cdot 10^{-4}$ [m], $L_{drift} = 10^{-3}$ [m]. Lie transforms are truncated to fifth order.

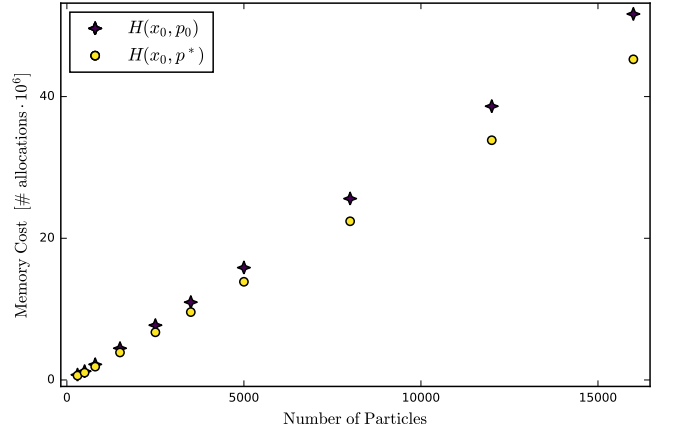


FIG. 3. Raw memory-allocation cost for multiparticle simulations with k and L parameters matching those of Fig. 2. Exponential Lie-operator (Eq. 20) series truncation order: 6. Number of simulated segments: 50.

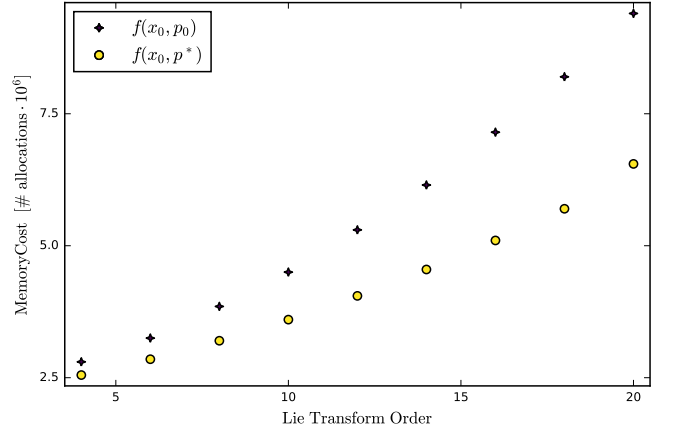


FIG. 4. Raw memory-allocation cost for multiparticle simulations with k and L parameters matching those of Fig. 2. Number of particles: 10,000. Number of simulated segments: 5.

appears to perform better. This can be justified on the assumption that either ρ_x^0 or ρ_p^0 remains approximately constant. That is

$$V_{xp} = \int \int \rho_x^L \rho_p^L dx_L dp_L = \int \int \rho_x^0 \rho_p^0 dx_0 dp_0 \quad (25)$$

$$\approx \oint_p \int \int \rho_x^L dx_L dp_L = \oint_p \int \int \rho_x^0 dx_0 dp_0,$$

when using $p_0 \rightarrow p^*$, where the phase-space volume V_{xp} is conserved via Liouville's theorem.

The momentum equivalent of Eq. 24

$$\rho_p^L = \frac{\rho_p^0}{\left| \frac{\partial x_L}{\partial x_0} \frac{\partial p_L}{\partial p_0} \right|_{x_0 \rightarrow x^*}} \quad (26)$$

also shows good agreement with the multiparticle case for high- k , low- L scenarios (Fig. 6). It should be noted, however, that the envelope approximation breaks down for

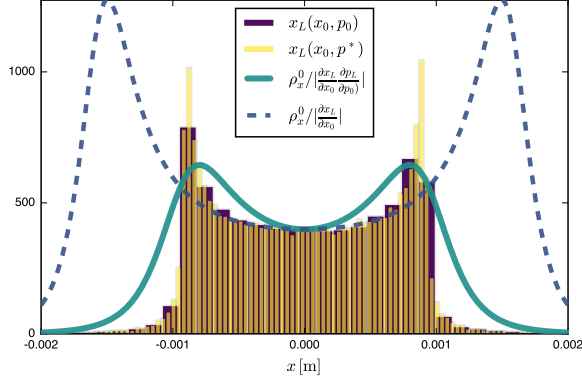


FIG. 5. Multiparticle and envelope octupole transformations in x_L (single kick) with $k = 9.73 \cdot 10^{-7} \text{ T} \cdot \text{m}^{-3}$, $L = 1 \cdot 10^{-2} \text{ m}$.

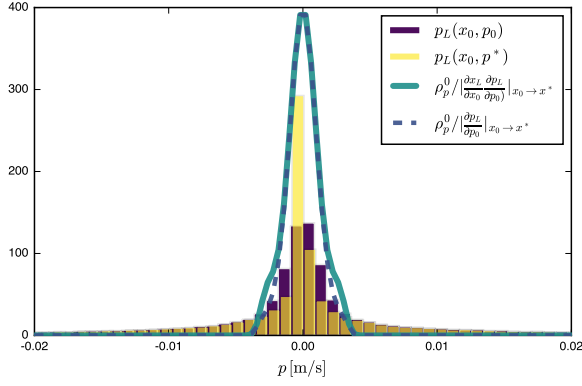


FIG. 6. Multiparticle and envelope octupole transformations in p_L (single kick) with $k = 1.93 \cdot 10^{-7} \text{ T} \cdot \text{m}^{-3}$, $L = 1 \cdot 10^{-2} \text{ m}$, single kick).

high- L cases (peak widths are generally overestimated). This discrepancy is unsurprising, given that either ρ_x^0 or ρ_p^0 must be taken as constant to use Eq. 25.

V. CONCLUSION

Approximating bivariate polynomials as monovariates is illustrated for the case of Lie transforms, where an output position is no longer necessarily dependent on momentum, and vice-versa. Since Lie transforms of non-linear Hamiltonians are inherently bivariate (i.e. coupled to both position and momentum variables), this approximation could substantially reduce the cost for simulating non-linear beamline elements or high-order errors. However, further testing is needed to gauge its effect on performance for 3D, full-machine simulations.

On this note, it is worth mentioning that if a generalized form of Eq. 13 were deduced, irregular initial distributions could be implemented, making this method more viable as an “as needed” speedup routine (i.e. only triggered for certain machine elements).

More importantly, this technique also presents a means for nonlinear tracking of phase-space density envelopes, which have computational requirements minimal enough for real-time tracking. In this regard, the use of Eq. 24 may be taken as a nonlinear extension to the thin-lens formalism.

VI. APPENDIX

Instructions for building a Julia environment in Jupyter notebooks, with accompanying code for reproducing these results, can be found at:

<https://github.com/benfolson/dclapprx>

-
- [1] E Laface. Non-Linear Dynamics Model for the ESS Linac Simulator. *Proceedings of IPAC 2015, Richmond VA, USA*, May 2015.
 - [2] B Folsom and E Laface. Fast tracking of nonlinear dynamics in the ess linac simulator via particle-count invariance. In *7th International Particle Accelerator Conference (IPAC'16), Busan, Korea, May 8-13, 2016*, pages 3080–3082. JACOW, Geneva, Switzerland, 2016.
 - [3] Yosuke Yuri, Nobumasa Miyawaki, Tomihiro Kamiya, Watalu Yokota, Kazuo Arakawa, and Mitsuhiro Fukuda. Uniformization of the transverse beam profile by means of nonlinear focusing method. *Physical Review Special Topics-Accelerators and Beams*, 10(10):104001, 2007.
 - [4] F Meot and T Aniel. Principles of the non-linear tuning of beam expanders. *Nuclear Instruments and Methods in Physics Research Section A: Accelerators, Spectrometers, Detectors and Associated Equipment*, 379(2):196–205, 1996.
 - [5] Alex J Dragt. *Lie methods for nonlinear dynamics with applications to accelerator physics*. University of Maryland, Center for Theoretical Physics, Department of Physics, 2015.
 - [6] Jeff Bezanson, Stefan Karpinski, Viral B Shah, and Alan Edelman. Julia: A fast dynamic language for technical computing. *arXiv preprint arXiv:1209.5145*, 2012.
 - [7] David Delaat. Multipoly.jl; sparse multivariate polynomials in julia. <https://github.com/daviddelaat/MultiPoly.jl>, 2016.